The characteristics of the 2022 Tonga volcanic tsunami in the Pacific Ocean

Gui Hu[1], Linlin Li[1,2], Zhiyuan Ren[3], Kan Zhang[1]

1. Guangdong Provincial Key Laboratory of Geodynamics and Geohazards, School of Earth Sciences and Engineering, Sun Yat-sen University, Guangzhou, China

2. Southern Marine Science and Engineering Guangdong Laboratory (Zhuhai), Zhuhai, China

3. Department of Civil and Environmental Engineering, National University of Singapore, Singapore.

Correspondence to: Linlin Li (lilinlin3@mail.sysu.edu.cn)

Abstract. On 15th January 2022, an exceptional eruption of Hunga Tonga–Hunga Ha'apai volcano generated atmospheric and tsunami waves that were widely observed at oceans globally, gaining a remarkable attention to scientists in related fields. The tsunamigenic mechanism of this rare event remains an enigmatic due to its complexity and lacking of direct underwater observations. Here, to explore the tsunamigenic mechanisms of this volcanic tsunami event and its hydrodynamic processes in the Pacific Ocean, we conduct tsunami waveform and spectral analyses of the waveform recordings at 116 coastal gauges and 38 deep-ocean buoys across the Pacific Ocean. Combined with the constraints of some representative barometers, we obtain the plausible tsunamigenic origins during the volcano activity. We identify four distinct tsunami wave components generated by air-sea coupling and seafloor crustal deformation. Those tsunami components are differentiated by their different propagating speeds or period bands. The first-arriving tsunami component with ~80–100 min period was from shock waves spreading at a velocity of ~1000 m/s in vicinity of the eruption. The second component with extraordinary tsunami amplitude in deep sea was from Lamb waves. The Lamb wave with ~30–40 min period radically propagated outward from the eruption site with spatially decreasing propagation velocities from ~340 m/s to ~315m/s. The third component with ~10–30 min period was probably from some atmospheric gravity wave modes propagating faster than 200 m/s but slower than Lamb waves. The last component with ~3–5 min period originated from partial caldera collapse with dimension of ~0.8–1.8 km. Surprisingly, the 2022 Tonga volcanic tsunami produced long oscillation in the Pacific Ocean which is comparable with those of the 2011 Tohoku tsunami. We point out that the long oscillation is not only associated with the resonance effect with the atmospheric acoustic-gravity waves, but more importantly the interactions with local bathymetry. This rare event also calls for more attention to the tsunami hazards produced by atypical tsunamigenic source, e.g., volcanic eruption.

1. Introduction

On 15 January 2022 at 04:14:45 (UTC), a submarine volcano erupted violently at the uninhabited Hunga Tonga-Hunga Ha'apai (HTHH) island at 20.546°S 175.390°W (USGS, 2022). The volcano is located ~67 km north of Nuku'alofa, the capital of Tonga (NASA, 2022) (Figure 1). The blasts launched plumes of ash, steam, and gas ~58 km high into stratosphere (Yuen et al., 2022) which not only blanketed nearby islands in ash (Duncombe, 2022; NASA, 2022), but caused various atmospheric acoustic-gravity wave modes (AGWs) of various scales, e.g., Lamb waves from atmospheric surface pressure disturbance associated with the eruption (Liu and Higuera, 2022; Adam, 2022; Kubota et al., 2022; Matoza et al., 2022). Tsunami with conspicuous sea level changes were detected by coastal tide gauges and Deep-ocean Assessment and Reporting of Tsunamis (DART) buoy stations in the Pacific (Figure 1), the Atlantic, and Indian Oceans as well as the Caribbean and Mediterranean seas (Carvajal et al., 2022; Kubota et al., 2022; Ramírez-Herrera et al., 2022), while the large waves were mainly concentrated in the Pacific Ocean, like coastlines of New Zealand, Japan, California, and Chile (Carvajal et al., 2022). The event caused at least 3 fatalities in Tonga. Two people drowned in northern Peru when ~2 m destructive tsunami waves inundated an island in the Lambayeque region, Chile (Edmonds, 2022).

Satellite images revealed that the elevation of HTHH island has gone through dramatic change before and after the mid-January 2022 eruption. Previously, after the 2015 eruption, the two existing Hunga Tonga and Hunga Ha'apai Islands were linked together. The volcanic island rose 1.8 km from the seafloor where it stretched ~20 km across and topped a underwater caldera ~5 km in diameter (Garvin et al., 2018; NASA, 2022). After the violent explosion on 15 January 2022, the newly formed island during 2015 was completely gone, with only small tips left in far southwestern and northeastern HTHH island (NASA, 2022). HTHH volcano lies along the northern part of Tonga–Kermadec arc, where the Pacific Plate subducts under the Indo-Australian Plate (Billen et al., 2003). The convergence rate (15~24 cm/year) between the Tonga-Kermadec subduction system and the Pacific plate is among the fastest recorded plate velocity on Earth, forming the second deepest trench around the globe (Satake, 2010; Bevis et al., 1995). The fast convergence rate contributes to the frequent earthquakes, tsunamis and volcanic eruptions in this region historically (Bevis et al., 1995). The 2022 HTHH volcano is part of a submarine-volcano chain that extends all the way from New Zealand to Fiji (Plank et al., 2020). HTHH volcano had many notable eruptions before 2022 since its first historically recorded eruption in 1912, i.e., in 1937, 1988, 2009, 2014-2015 (Global Volcanism Program, https://volcano.si.edu).

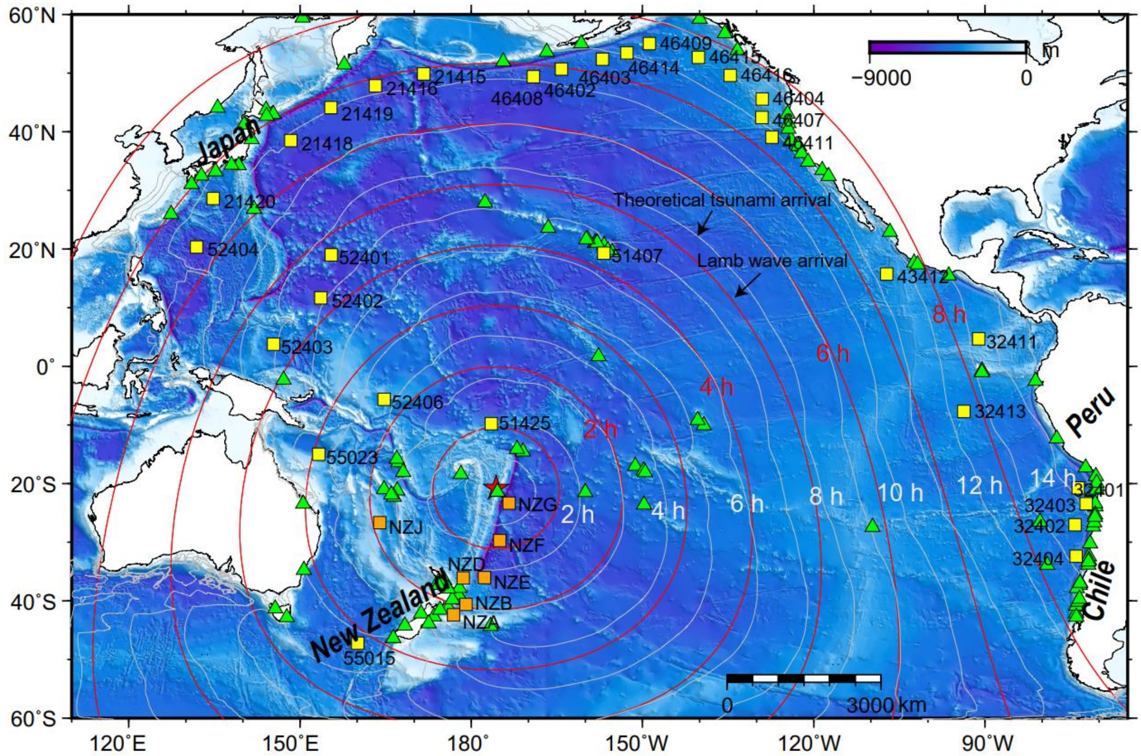

Figure 1. The spatial distribution of the eruption site (red star), DART stations (squares), tide gauges (triangles) and the calculated tsunami arrival times. White contours indicate the modelled arrival times of conventional tsunami. Red contours indicate the estimated arrival times of Lamb waves (see how we derive these contours in section 3.1).

The 2022 HTHH eruption is the first volcanic event which generates worldwide tsunami signatures since the 1883 Krakatau event (Matoza et al., 2022; Self and Rampino, 1981; Nomanbhoy and Satake, 1995). The tsunamigenic mechanism of this rare volcanic eruption-induced tsunami is still poorly understood due to its complex nature and the deficiencies of near-field seafloor surveys. Various tsunami generation mechanisms have been proposed so far based on the observations of ground-based and spaceborne geophysical instrumentations (Kubota et al., 2022; Matoza et al., 2022; Carvajal et al., 2022). The mechanisms are closely associated with the air-sea coupling with atmospheric waves. Atmospheric waves propagating in the atmospheric fluid are generated by different physical mechanisms (Gossard and Hooke, 1975a). Lamb wave is a horizontally propagating acoustic waves in Lamb mode which is trapped at the earth's surface with group velocities close to the mean sound velocity of the lower atmosphere (e.g. Lamb, 1932). Atmospheric gravity wave is triggered when air molecules in the atmosphere are disturbed vertically other than horizontally (e.g. Le Pichon et al., 2010). Nonlinear propagation of atmospheric wave may cause period lengthening and the formation of shock-wave (Matoza et al., 2022). The most-mentioned mechanism of the tsunami is the fast-traveling atmospheric Lamb wave generated by the atmospheric pressure rise of ~2 hPa during the eruption. The Lamp wave circled the Earth for several times with travelling speed close to that of the sound wave in the lower atmosphere, leading to globally observed sea level fluctuations (Adam, 2022; Duncombe, 2022; Kubota et al., 2022; Matoza et al., 2022) (Figure 1). The second mechanism is suggested to be a variety of other acoustic-gravity wave modes (Adam, 2022; Matoza et al., 2022; Themens et al., 2022; Zhang et al., 2022). The third mechanism may be related to the seafloor crustal deformation induced by one or more volcanic activities in the vicinity of the eruption site (e.g., pyroclastic flows, partial collapse of the caldera) (Carvajal et al., 2022) , which are more responsible for the near-field tsunamis with theoretical tsunami speeds.

To investigate the possible tsunamigenic mechanisms and detailed hydrodynamic behaviors of this rare volcanic tsunami event, in this study, we collect, process and analyze the sea level measurements from 116 tide gauge and 38 DART buoys in the Pacific Ocean (shown in Figures 1 and 2). We first do statistical analysis of the tsunami waveforms to estimate the propagating speed of the Lamb wave and to understand the tsunami wave characteristics in the Pacific Ocean through demonstrating the tsunami wave properties, i.e., arrival times, wave heights and durations. We then conduct wavelet analysis for representative DART buoys and tide gauges respectively to explore tsunamigenic mechanisms of the event and to better understand its hydrodynamic processes in the Pacific Ocean. Aided by wavelet analysis of corresponding barometers near the selected DART buoys and comparison with tsunami records of the 2011 Tohoku tsunami, we are able to piece together all the analysis and demonstrate that the 2022 HTHH tsunami was generated by air-sea coupling with a wide range of atmospheric waves with different propagating velocities and period bands, and seafloor crustal deformation associated with the volcanic eruption. We demonstrate as well that the tsunami was amplified at the far-field Pacific coastlines where the local bathymetric effects play a dominant role in tsunami scale.

2. Data and Methods

2.1 Data

We collected high-quality sea level records across the Pacific Ocean at 38 DART buoys (in which 31 stations from https://nctr.pmel.noaa.gov/Dart/, 7 stations from https://tilde.geonet.org.nz/dashboard/) and

116 tide gages from IOC (The Intergovernmental Oceanographic Commission, http://www.ioc-sealevelmonitoring.org) (Figure 1). The epicentral distances of tide gauges and DART buoys range between 74–10790 km and 375–10414 km, respectively. The sampling rates of DART buoys are changing over time. Passing of tsunami event generally can trigger the DART system to enter its high frequency sampling mode (15 seconds or 1 min) from normal frequency mode (15 min) (www.ndbc.noaa.gov/dart). In contrast, sampling rates of normal tide gauges at coasts are uniform with sampling interval of 1 min. The sampling interval of both DART and tide gauges is preprocessed to 15 seconds. Firstly, we eliminate abnormal spikes and fill gaps by linear interpolation. Secondly, we applied a fourth-order Butterworth-Highpass filter with a cut-off frequency of 3.5 e-5 Hz (~ 8 hours) to remove the tidal components (Figure 2) (Heidarzadeh and Satake, 2013). After the two steps, quality control step is conducted to select high-quality data, in which we delete waveforms with spoiled data or massive data loss due to equipment failure, or with the maximum tsunami heights of tide gauges less than 0.2 m, then the selected data will be ready for further statistics and spectral analysis. We also collect and analyze the atmospheric pressure disturbance data recorded by some representative barometers. The sampling rates of the barometers is generally uniform with a sampling rate of 1 min except for some stations in New Zealand with interval of 10 min. Considering the sample rate, we employ a fourth-order Butterworth-Bandpass filter with period ranging between 2–150 min for wavelet analysis of the barometers with 1 min sample rate, while we apply the fourth-order Butterworth-Bandpass filter with range of 30–150 min to long-period waveform display based on two reasons. (1) The barometer data we use for the analysis include some in New Zealand with 10 min sample rate; (2) Filtering out the short-period waves helps highlight long-period tsunami wave components.

The tsunami waveforms recorded by DART buoys which are installed offshore in the deep water are expected to contain certain characteristics of the tsunami source (Wang et al., 2020, 2021). The waveforms recorded by tide gauge distributed along coastlines are significantly influenced by local bathymetry/topography which are used for investigating bathymetric effect on tsunami behaviors (Rabinovich et al., 2017, 2006; Rabinovich, 2009). Therefore, we use the DART data for source-related analysis and choose some tide gauge data to investigate the tsunami behaviors at the Pacific coastlines.

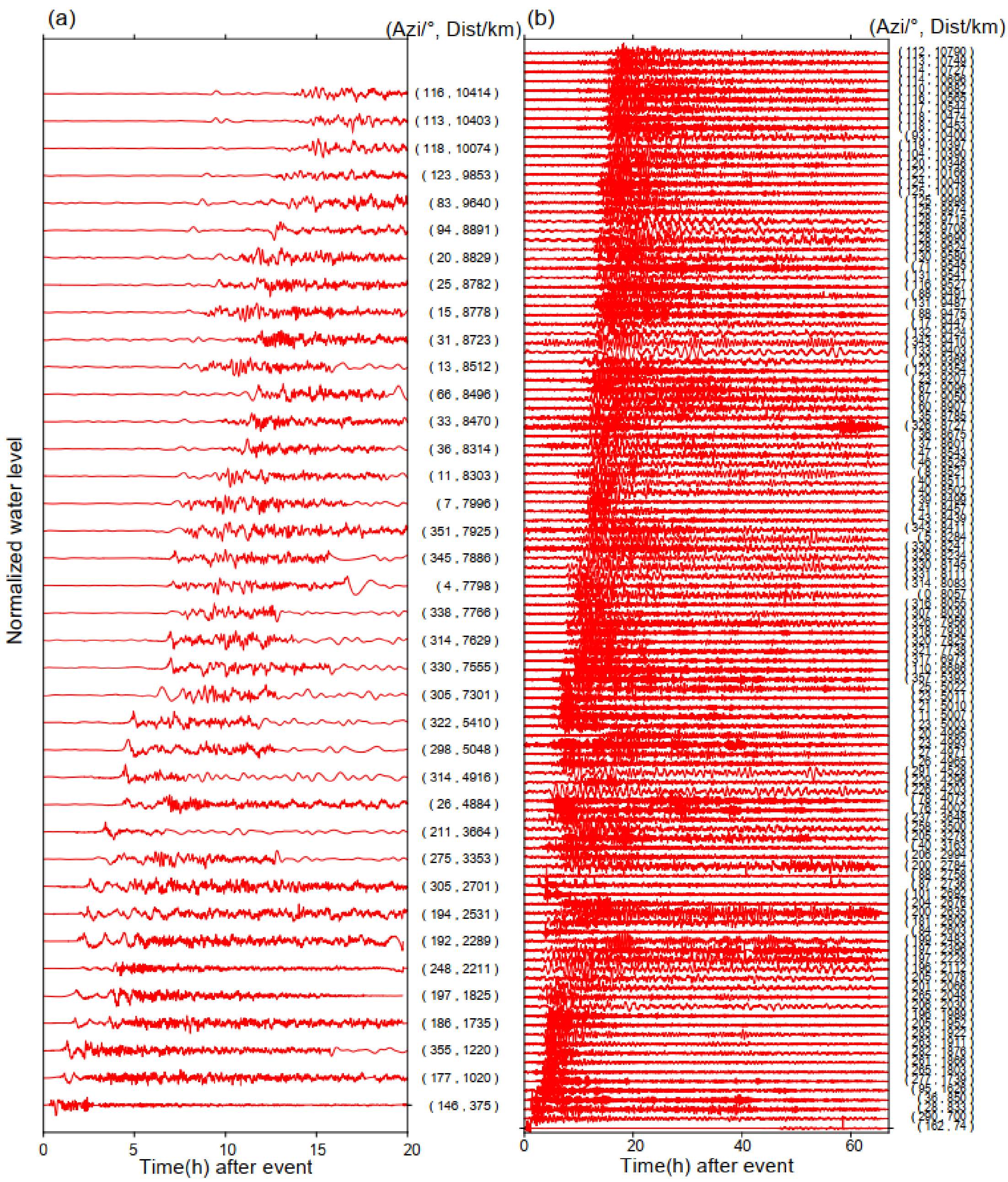

Figure 2. Detided tsunami waveforms at (a) DART buoys and (b) tide gauges. Waveforms in both subplots are shown in ascending distance. Azi stands for azimuth. The data are normalized with respect to the largest amplitude of each tide gauge.

2.2 Tsunami Modelling

We use a numerical tsunami modelling package JAGURS (Baba et al. 2015) to simulate the tsunami propagation of the 2022 HTHH event and obtain the theoretical tsunami arrival time based on the shallow water wave speed (white contours in Figure 1). The code solves linear Boussinesq-type equations in a spherical coordinate system using a finite difference approximation with the leapfrog method. We specify a unit Gaussian-shaped vertical sea surface displacement at the volcanic base as the source of conventional tsunami. For a unite source i with center at longitude φ_i and latitude θ_i, the displacement distribution $Zi(\varphi,\theta)$ can be expressed as:

$$Zi(\varphi,\theta) = exp[-\frac{(\varphi-\varphi_i)^2+(\theta-\theta_i)^2}{2\sigma}] \quad (1)$$

Where we set characteristic length σ as 5 km (NASA, 2022). The bathymetric data is resampled from the GEBCO 2019 with 15 arc-sec resolution (The General Bathymetric Chart of the Oceans, downloaded from https://www.gebco.net).

2.3 Spectral Analysis of Tsunami Waves

To investigate the temporal changes of the dominant wave periods, we conduct continuous wavelet transformation (frequency-time) analyses for some representative DART buoys, tide gauges and barometers, in which wavelet Morlet mother function is implemented (Kristeková et al., 2006). The first 32-hour time series of DART buoys and barometers after the eruption (at 04:14:45 on 15 January 2022) are used for source-related wavelet analysis. The first 48-hour time series of tide gauges after the eruption are employed for hydrodynamics-related wavelet analysis at coastlines. We adopt the Averaged-Root-Mean-Square (ARMS) method as a measure of absolute average tsunami amplitude with a moving time window of 20 min to calculate the tsunami duration (Heidarzadeh and Satake, 2014). We define the time durations as the time period where ARMS levels of tsunami waves are above those prior to the tsunami arrivals.

3. Results

3.1 The decreasing propagation velocities of the Lamb Wave

Although many types of atmospheric waves were generated by the 2022 HTHH eruption, the most prominent signature was the Lamb waves which were globally observed by ground-based and spaceborne geophysical instrumentations (Kulichkov et al., 2022; Liu et al., 2022; Lin et al., 2022; Matoza et al., 2022; Themens et al., 2022; Adam, 2022; Kubota et al., 2022). Interestingly, we notice that a wide range of the velocities from 280 m/s to 340 m/s were proposed through observations and Lamb wave modelling (e.g., Kubota et al., 2022; Lin et al., 2022; Matoza et al., 2022; Themens et al., 2022). The travelling velocity of Lamb waves in real atmosphere is affected by temperature distributions, winds and dissipation (Otsuka, 2022). To investigate whether the propagation speeds of the lamb wave change in space and time, we analyze the waveforms recorded by the DART buoys in the Pacific Ocean. DART buoy with pressure sensor deployed at the ocean's bottom records the sea level change that is transferred from pressure records in Pascals, instead of direct water height. For the 2022 HTHH tsunami event, the pressure fluctuation at DART buoy is a superposition of the pressure changes caused by tsunami and the Lamb wave (Kubota et al., 2022). The Pacific DART buoys recorded the most discernible air-sea coupling pulse in deep ocean with Lamb waves that arrived earlier than the theoretical tsunamis (Figure 1). The tsunami waveforms recorded by tide gauges did not clearly detect the tsunami signals associated with the Lamb waves, therefore are not sufficient for further analysis (Figure 2). Thus, we estimate the speed of Lamb waves using the waveforms recorded by the Pacific DART buoys. The Lamb wave arrivals are limited within arrival time range from possible velocities of 280–340 m/s. The time points at which the tsunami amplitudes first exceed 1 e-4 m above sea level are defined as Lamb wave arrivals. By carefully fitting the arrivals with different constant velocities, we illustrate the velocities of Lamb wave were generally uniform, but slightly decrease with the increase of propagation distance (Figure 3). The Lamb waves initially propagated radially at speed of ~340 m/s before slowing to ~325 m/s after reaching ~3400 km, and further decreasing to ~315 m/s at 7400 km. In an isothermal troposphere assumption, the phase velocity of the Lamb wave (C_L) can be estimated with the following equation (Gossard and Hooke, 1975b):

$$C_L = \sqrt{\frac{\gamma.R.T}{M}} \qquad (2)$$

Where γ =1.4 (air specific heat ratio corresponding to atmospheric temperature), R = 8314.36 J kmol-1 K-1 (the universal gas constant), M = 28.966 kg kmol-1 (molecular mass for dry air) are constant for the air, T is the absolute temperature in kelvin. Thus, Lamb wave velocity is mainly affected by the air temperature, meaning the travelling velocity of lamb waves might decrease when propagating from regions with high temperature towards those with low temperatures, e.g., the north pole. By assuming a set of possible temperatures in January (Table 1), we calculated the velocities C_L could range between 312–343 m/s when temperatures vary between -30–20 °C. Therefore, the decreased velocity of the Lamb waves could be a consequence of cooling of the air temperature.

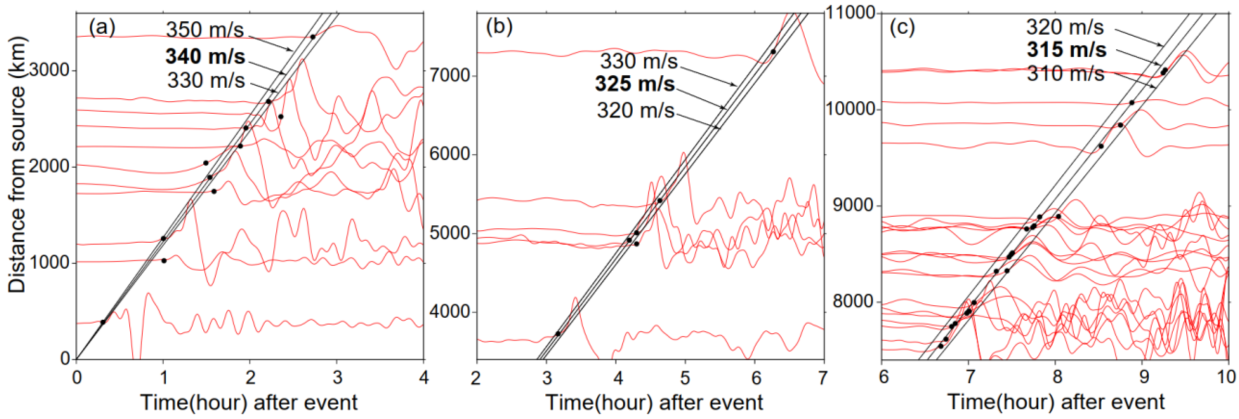

Figure 3. Fitting the arrival times of normalized Lamb-induced tsunami waveforms with different velocities. Black dots mark the arrival times of the Lamb waves. Black lines represent velocities.

Table 1. Estimated Lamb wave velocities in an isothermal troposphere assumption

Celsius temperature (°C)	thermodynamic temperature (K)	C_L (m/s)
20	293.15	343.14
10	283.15	337.23
0	273.15	331.21
-10	263.15	325.19
-20	253.15	318.86
-30	243.15	312.49

3.2 Tsunami features observed by DART buoys and Tide gauges

The statistics of tsunami heights and arrival times recorded at 38 DART buoys and 116 tide gauges across the Pacific Ocean are used to interpret the tsunami characteristics. The comparison of the statistical characters between DART and tide gauge observations yields some useful information of the hydrodynamic process of tsunami propagation and help identify tsunami wave components with different traveling velocities.

The average value of the maximum tsunami wave height (trough-to-crest) for the 116 tide gauge stations is ~1.2 m. Figure 4a shows tide gauges with large tsunami heights exceeding 2 m are mainly distributed in coastlines with complex geometries (Figure S1a), such as gauges at New Zealand, Japan, and north and south America. For example, the largest tsunami height among tide gauges is 3.6 m at a bay-shaped coastal area Chañaral in Chile (Figure S1b). In sharp contrast to tide gauges, the maximum tsunami heights of most Pacific DART buoys are less than 0.2 m. The largest tsunami height in the DART buoys is only ~0.4 m recorded at the nearest one, 375 km from the volcano (Figure 4b). The comparison between DART buoys and tide gauges indicate that the direct contribution of air-sea coupling to the tsunami heights is probably in the level of tens of centimeters (Kubota et al., 2022). The meter-scale tsunami heights at the coastlines suggest the bathymetric effect could play a major role during tsunami propagation. In respect to the arrival of maximum tsunami waves, the time lags between Lamb waves and the maximum heights of tide gauges mainly range between ~0–10 h (Figure 4c). The delayed times of ~10 h are observed in New Zealand, Hawaii, and west coast of America (Figure 4c), suggesting the interaction between tsunami waves and local topography/bathymetry delays the arrival of the maximum waves (e.g., Hu et al., 2022). For example, the delayed maximum tsunami height can be attributed to the edge waves (Satake et al., 2020) and resonance effect (Wang et al., 2021) from tsunami interplays with bays/harbors, islands, and continental shelves of various sizes. The significant regional dependence of the coastal tsunami heights and the time lags of the maximum tsunami waves can be attributed to the complexity of local bathymetry, such as continental shelves with different slopes, and harbor/bay with different shapes and sizes (Satake et al., 2020). On the other hand, for tsunami events with earthquake origins (e.g. Heidarzadeh and Satake, 2013), the first waves recorded by DART buoys are normally observed as the largest wave since DART buoys are located in the deep sea and less influenced by bathymetric variation. In the case of Tonga tsunami event, we observe the inconsistency between the arrivals of the Lamb wave-induced tsunami waves and the maximum tsunami heights (Figure 4d). The time lags of the maximum waves of DART buoys present a coarsely increasing tendency with the increasing distance from the volcano, which indicates the contribution of other tsunami generation mechanism propagating with a uniform but lower speed than Lamb wave.

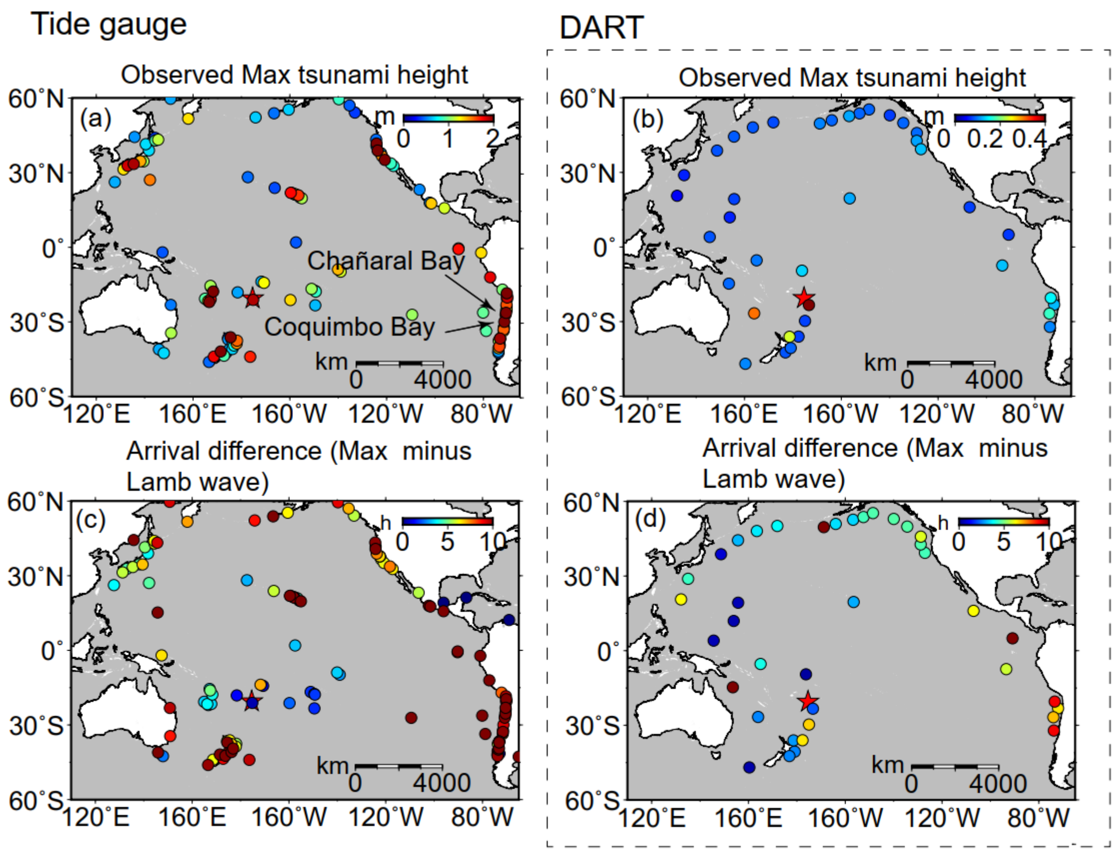

Figure 4. The spatiotemporal signatures of the 2022 HTHH tsunami across the Pacific Ocean. (a) Observed the maximum tsunami height (trough-to-crest height) of tide gauges. (c) Arrival differences between the maximum tsunami height of tide gauges and Lamb waves. (b) and (d) are the same as (a) and (c) but for DART buoys.

3.3 Tsunami components identified from wavelet analysis

The statistical analysis of tsunami waveforms at tide gauges and DART buoys suggest the tsunami waves likely contain several components with different source origins. To further identify these tsunami components, we conduct wavelet analysis for tsunami waveforms recorded by representative DART buoys and air pressure waveforms recorded by selected barometers. We demonstrate the analysis result through the frequency-time (f-t) plot of wavelet which shows how energy and period vary at frequency and time bands (Figure 5 and Figure 6). Tsunami components have clear signatures in all f-t plots as the energy levels are quite large when they arrive. Figure 5 shows the wavelet analysis of six DART buoys located in the vicinity of the eruption site (<3664 km). Figure 6 show the wavelet analysis of ten DART buoys located in the Pacific rim which are far away from the source location. We observe three interesting phenomena: 1) most of the tsunami wave energy is concentrated in four major period bands, i.e., 3–5 min, ~10–30 min, ~30–40 min, and ~80–100 min; 2) The significant tsunami component with period band of 3-5 mins are recorded by stations between the eruption site and the north tip of the New Zealand; 3) There exists one exceptional tsunami component with longer wave period of ~80–100 min mainly recorded in the Tonga, the New Zealand and Hawaii, which travels even faster than the Lamb waves.

To further explore the source mechanism of these tsunami components, we take advantage of the published information related to different propagating velocities of atmospheric gravity waves (Kubota et al., 2022) and add four kinds of propagating velocities as criteria to differentiate the tsunami arrivals from different sources (Figure 5 and Figure 6). The first reference speed is 1000 m/s related to the radically propagating atmospheric shock waves near the source region (Matoza et al., 2022; Themens et al., 2022). The second one is the velocities of Lamb wave ranging between 315–340 m/s derived from the aforementioned analysis in section 3.1 (Figure 3). The third one is 200 m/s corresponding to the lower limit of atmospheric gravity wave modes other than Lamb waves which were also excited by the volcanic eruptions (Kubota et al., 2022). The last is the arrival time of conventional tsunami given by tsunami modelling (Figure 1). The theoretical velocity of conventional tsunami is significantly nonuniform spatially as compared with those of the atmospheric waves. The conventional tsunami propagation speed is determined by the water depth along the propagation route. The velocity of non-dispersion shallow-water waves (C_H) in the ocean is given by:

$$C_H = \sqrt{g.H} \tag{3}$$

Where g is gravity acceleration (9.81m/s^2), H is the water depth. The propagation velocities of tsunami are ~296–328 m/s in the deepest trenches on earth (i.e., ~11 km in Mariana Trench and ~9 km in Tonga Trench). The velocities decrease quickly to only ~44 m/s at ~200 m depth along the edge of continental shelf. With the average depth of ~4–5 km, the average velocities in the Pacific Ocean range between ~200–224 m/s. Thus, theoretical tsunami velocities present significant slowness and variability. We delineate the arrival times of the four reference speeds in Figures 5 and 6.

One particularly remarkable phenomenon is that the wave component with period of ~80–100 min propagated at a very fast speed of ~1000 m/s in the vicinity of the HTHH site, i.e., New Zealand and Hawaii (e.g., stations 52406, NZJ, NZE, 51425 in Figure 5, and 51407 in Fig. 6). We infer that the tsunami component within ~80–100 min period band was likely produced by the atmospheric shock waves during the initial stage of the volcanic eruption and spatially only cover the near-source region. To verify this observation, we select 16 representative barometers located in the near-source region and far-field area for wavelet analysis (see the locations in Figure 5 and Figure 6). Figure 7 shows the waveforms of atmospheric pressure at selected locations and Figure 8 provides the frequency-time (f-t) plot of wavelet analysis of some representative barometers. Interestingly, we are able to discern the air pressure pulses prior to Lamb waves at barometers in New Zealand (the two columns on the left in Figure 7), although such signals are not detectable in waveforms recorded by barometers far from the source (the two columns on the right in Figure 7). The spatial distribution of such unusual pressure changes suggest that the fast travelling shock waves were only limited in the near-source region, as reflected in the travelling ionospheric disturbances (Matoza et al., 2022; Themens et al., 2022). Additionally, we also see that the long period signals of ~80–100 min appear in DART buoys far away from the eruption site. Such signals may be related with the long-period gravity waves (Matoza et al., 2022).

The tsunami components at period band of ~30–40 min can be readily associated with Lamb waves because the arrival times of the tsunami waves and Lamb waves have excellent match, as shown in the tsunami data recorded by DART buoys (e.g., NZJ and 51425 in Figure 5; 51407, 32401 and 32413 in Figure 6) and pressure data by barometers (Figure 8).

For the tsunami components with the period band of ~10–30 min, although the arrivals of ~10–30 min tsunami components cover some theoretical tsunami arrival times, they do not consistently match. The tsunami components occurring within the time period between Lamb waves and the lower gravity waves' velocities has a good agreement with the velocity range of several atmospheric gravity wave modes (Matoza et al., 2022; Themens et al., 2022; Kubota et al., 2022). Similarly, the air pressure data also show energy peaks at ~10–30 min period band, which is consistent with the tsunami data (Figure 8). Such consistency further verifies the contribution of atmospheric gravity waves to the volcanic tsunami.

The tsunami components with the shortest period of ~3–5 min (stations NZE, NZF, NZG and NZJ; marked with black dashed squares in Figure 5) are only observed at DART records near the eruption location. Meanwhile, the arrival times of these components agree well with the modelled arrivals of conventional tsunami. Thus, we believe the observed shortest period band should originate from the seafloor crustal deformation. We further infer that this component could be generated by the partial underwater caldera collapse and/or subaerial/submarine landslide failures associated with 2022 HTHH volcanic eruption.

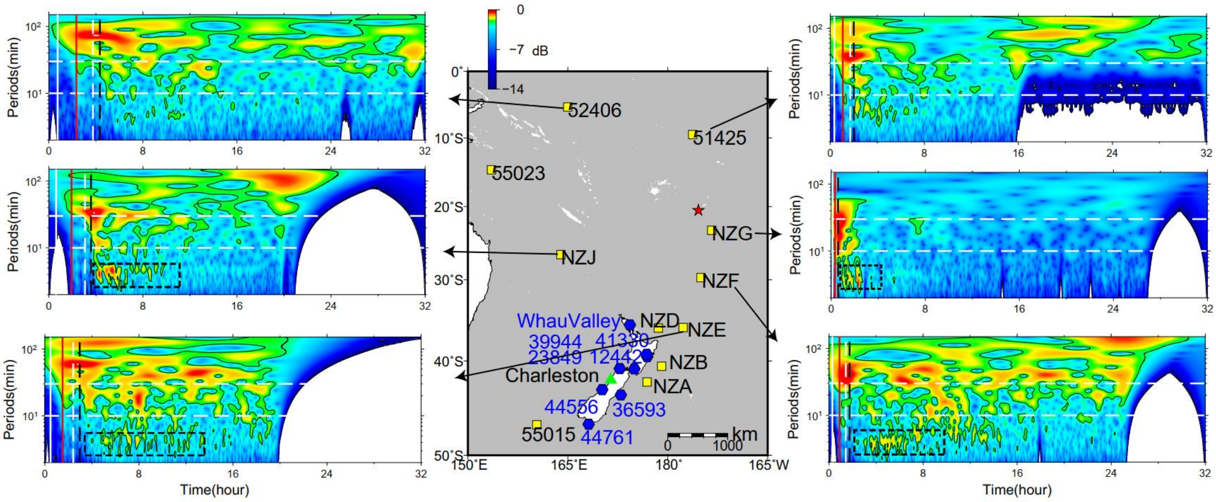

Figure 5. Wavelet analysis of representative DART buoys in the vicinity of the HTHH volcano. In each sub-plot, the solid vertical white lines mark the arrival time with travelling velocity of 1000 m/s. The solid vertical red lines mark the arrivals of Lamb waves. The dashed vertical white lines mark lower limit of AGWs' velocity of 200 m/s (Kubota et al., 2022). The dashed vertical black lines represent the theoretical tsunami arrivals. The dashed horizontal white lines mark two reference wave periods of 10 min and 30 min. The blue hexagons represent the locations of barometers. Green triangle makes the location of the tide gauges at Charleston. Decibel (dB) is calculated from: dB = 10 log(A/A_0), where A is wavelet power, A_0 is a reference wavelet power of the maximum one (Thomson and Emery, 2014).

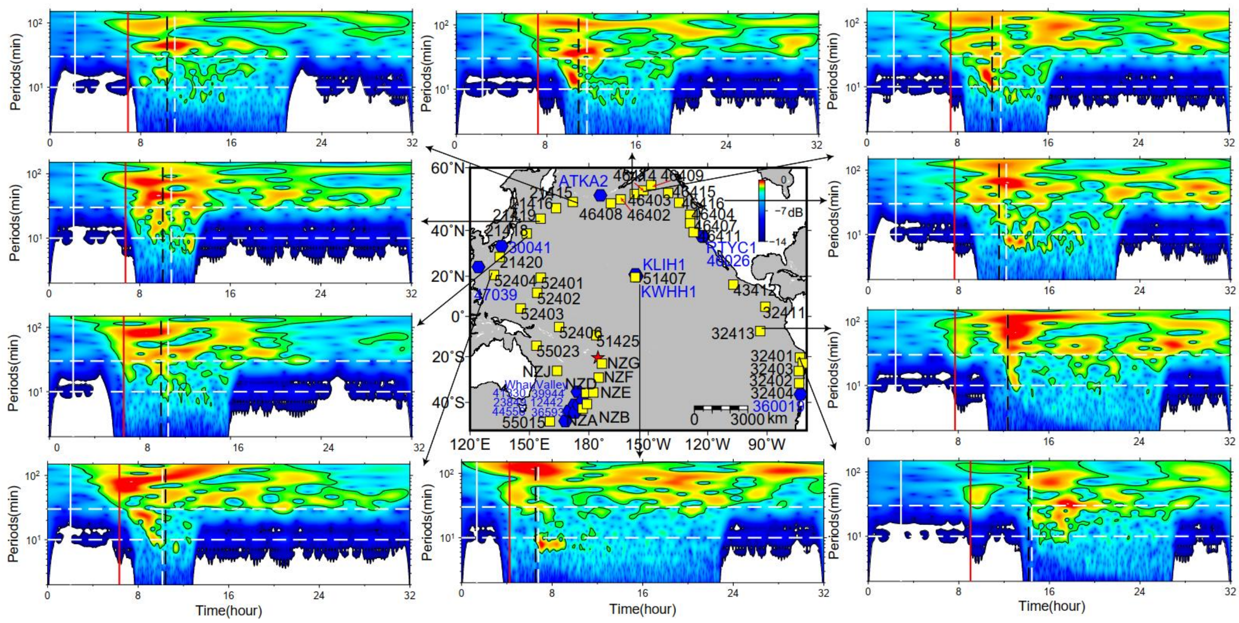

Figure 6. Wavelet analysis of representative DART buoys far away from the HTHH volcano. In each sub-plot, the solid vertical white lines mark the arrival time with travelling velocity of 1000 m/s. The solid vertical red lines mark the arrivals of Lamb waves. The dashed vertical white lines mark lower limit of AGWs' velocity of 200 m/s. The dashed vertical black lines represent the theoretical tsunami arrivals. The dashed horizontal white lines mark two reference wave periods of 10 min and 30 min. The blue hexagons represent the locations of barometers.

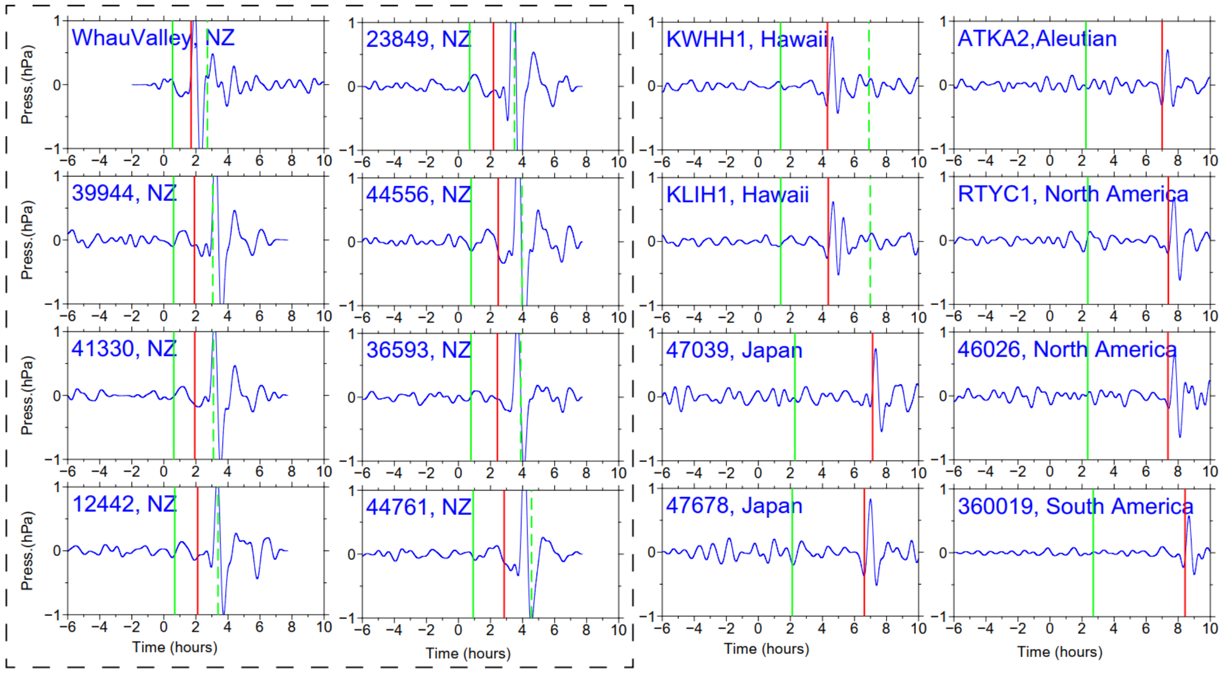

Figure 7. Shockwave-related atmospheric pressure waveforms of selected barometers in the Pacific Ocean. All traces have been filtered between 30 min and 150 min. In each sub-plot, the solid vertical green lines mark the arrival time with travelling velocity of 1000 m/s. The solid vertical red lines mark the arrivals of Lamb waves. The dashed vertical green lines mark lower limit of AGWs' velocity of 200 m/s.

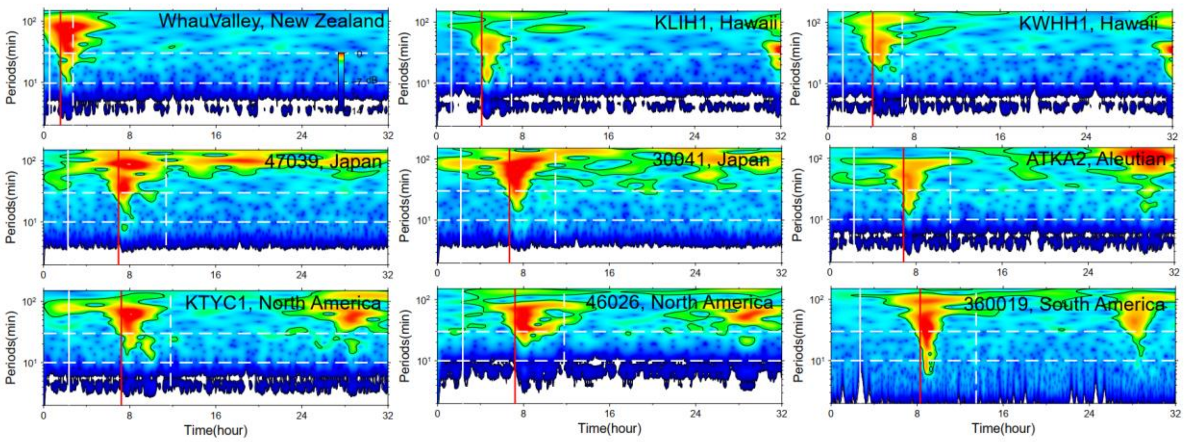

Figure 8. Wavelet analysis of some representative barometers. In each sub-plot, the solid vertical white lines mark the arrival time with travelling velocity of 1000 m/s. The solid vertical red lines mark the arrivals of Lamb waves. The dashed vertical white lines mark lower limit of AGWs' velocity 200 m/s. The dashed horizontal white lines mark three reference periods of 10 min and 30 min.

4. Discussion

4.1 Tsunami from Caldera Collapse and Its Long-distance Traveling Capability

The tsunami wave energy distributed in different period bands is identified with reference arrival times. The tsunami component with 3–5 min period is most likely generated by seafloor crustal deformation in the volcanic site, but specific mechanism is not determined. A variety of possible scenarios associated with the eruption could be responsible for the near-field tsunami waves, such as volcanic earthquakes, pyroclastic flows entering the sea, underwater caldera flank collapse, and subaerial/submarine failures (Self and Rampino, 1981; Pelinovsky et al., 2005). To further investigate the source mechanism, we apply a simplified model (Rabinovich, 1997) to estimate the probable dimension of tsunami source:

$$L = \frac{T\sqrt{gH}}{2} \quad (4)$$

Where L is the typical dimension (length or width) of the tsunami source, H is average water depth in the source area, g is the gravity acceleration, and T is primary tsunami period. By comparing with the post-2015 morphology of the HTHH caldera which was obtained through drone photogrammetry and multibeam sounder surveys, Stern et al. (2022) estimate that much of the newly-formed Hunga Tonga Island and the 2014/2015 cone were destroyed by the 2022 eruption, and the vertical deformation of Hunga Ha’apai Island is ~10–15 m (Stern et al., 2022). With no more quantitative constraint of the seafloor deformation, we tentatively assume H as 10–15 m, then the possible dimension of seafloor crustal deformation responsible for the small-scale tsunami could be in the scale of 0.8–1.8 km (Figure 9a). The estimated size is very likely from partial caldera collapse that usually has limited scale in volcanic site (Ramalho et al., 2015; Omira et al., 2022). If it is the case, the partial flank collapse could be located between Hunga Tonga and Hunga Ha'apai Islands.

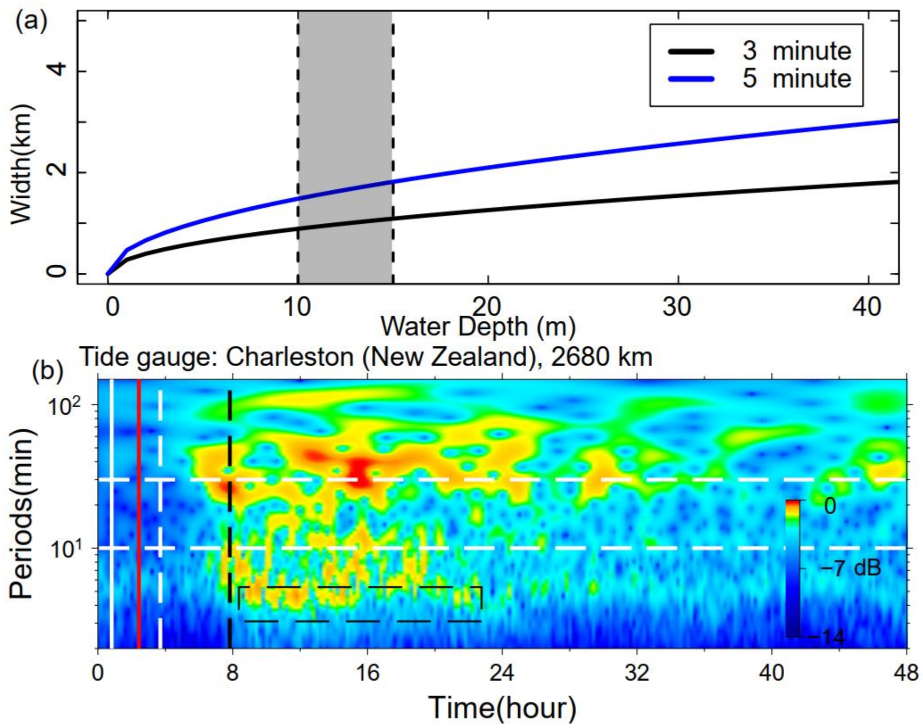

Figure 9. Mechanism of tsunami component with 3–5min period. (a) The source dimension estimated by equation 4. (b) Wavelet analysis of tide gauge at Charleston, New Zealand, 2680 km away from the eruption site. The solid vertical white line marks the arrival time with travelling velocity of 1000 m/s. The solid vertical red line marks the arrival of Lamb wave. The dashed vertical white line marks lower limit of AGWs' velocity 200 m/s. The dashed vertical black line marks the theoretical tsunami arrivals.

An interesting phenomenon is that the tsunami component with 3–5 min period can still be observed in a bay-shaped coastal area at Charleston in New Zealand (see the location in Figure 5) which is 2680 km away from the eruption site and maintains a high energy level lasting up to 14 h (Figure 9b). The long-traveling capability could be associated with the ~ 10000 m deep water depth of the Tonga Trench that keeps the source signals from substantial attenuation. In deep open ocean, the wavelength of a tsunami can reach two hundred kilometers, but the height of the tsunami may be only a few centimeters. Tsunami waves in the deep ocean can travel thousands of kilometers at high speeds, meanwhile losing very little energy in the process. The long oscillation can be attributed to the multiple reflections of the incoming waves trapped in the shallow-water bay at Charleston.

Generally, devasting tsunamis with long-distance travelling capability are mostly generated by megathrust earthquakes (Titov et al., 2005). Caldera collapses or submarine landslides with limited scale normally only generate local tsunamis, e.g., the 1998 PNG (Papua New Guinea) tsunami event (Kawata et al., 1999) and the 1930 Cabo Girão tsunami event (Ramalho et al., 2015). Therefore, it's exceptional that the tsunami component from scale-limited failure could travel at-least 2680 km away from the eruption site. It demonstrates that tsunamis from small-scale tsunamigenic source have the capability to travel long distance and cause long oscillation at favored condition, e.g., deep trench, ocean ridge and bay-shaped coasts.

4.2 The Possible Mechanisms of Long Tsunami Oscillation

An important tsunami behavior of the 2022 HTHH tsunami is the long-lasting oscillation ~ 3 days in the Pacific Ocean (Figure 10a), which is comparable to that of the 2011 Tohoku tsunami, ~4 days (Heidarzadeh and Satake, 2013). We demonstrate the duration time of the tsunami oscillation through ARMS (Averaged-Root-Mean-Square) approach that is a measure of absolute average tsunami amplitude in a time period. The long-lasting tsunami energy can be observed at many regions, such as the coasts of New Zealand, Japan, Aleutian, Chile, Hawaii, and west coasts of America. Several mechanisms could account for the long-lasting tsunami, including (1) Lamb waves circling the Earth multiple times (Amores et al., 2022; Matoza et al., 2022), (2) resonance effect between ocean waves and atmospheric waves (Kubota et al., 2022), and (3) bathymetric effect. We discuss the contribution of each mechanism in the following section.

To investigate the contribution of Lamb wave to the long-lasting tsunami, we compare the air pressure disturbances recorded by selected barometers together with the tsunami waveforms of nearby tide gauges (Figure 10b). While the barometers present discernible wave pulses at each Lamb wave's arrival, only the first Lamb wave triggered clear tsunami signal and no detectable tsunami signatures correspond to the following passage, suggesting the Lamb waves do not directly contribute to the long oscillation.

The resonance effects between ocean waves and atmospheric waves could contribute to the long oscillation on coastlines. Besides the Lamb wave, Watanabe et al., 2022 detected internal Pekeris wave which propagate with a slower horizonal phase speed of ∼245 m/s and gravity waves with even slower propagation speed by analyzing radiance observations taken from the Himawari-8 geostationary satellite. Atmospheric waves with such speeds are more likely to resonant with the conventional tsunami waves and provide continuous energy supply (Kubota et al., 2022).

To examine the role of local bathymetry in the long-lasting tsunami, we choose a well-studied and well-recorded event: the 2011 Mw 9.0 Tohoku tsunami as a reference event and compare the tsunami records of these two events at the same coastal stations. Although the two tsunami events were generated by completely different mechanisms, i.e., large-scale seafloor deformation for the Mw 9.0 megathrust earthquake (Mori et al., 2011) and fast-moving atmospheric waves for the Mw 5.8 volcanic eruption (Matoza et al., 2022), they both produced widespread transoceanic tsunamis which were well recorded in the Pacific DART buoys and tide gauges. In the near-field, the 2011 Tohoku earthquake produced runup up to 40 m at Miyako in the Iwate Prefecture in Japan's Tohoku region (Mori et al., 2011). The epicenter is approximately 70 km east coast of the Oshika Peninsula of Tohoku region. However, the 2022 HTHH tsunami produced only ~13 m runup in the near field from eyewitness accounts in Kanokupolu, 60 km from the volcano (Lynett et al., 2022). However, in the far-field (>1000 km), we observe comparable tsunami wave heights in certain coastal regions. Based on the tsunami records at 21 tide gauges surrounding the Pacific Ocean, Heidarzadeh & Satake (2013) calculated the average value of the maximum tsunami heights (trough-to-crest) of the 2011 Tohoku tsunami is 1.6 m with the largest height of 3.9 m at the Coquimbo Bay in Chile (Heidarzadeh and Satake, 2013). Coincidently, the statistics of 116 tide gauges in this study also suggest the average tsunami heights of the 2022 HTHH tsunami is around the same order, ~1.2 m, among which, the largest height is 3.6 m at Chañaral Bay in Chile. Interestingly, in the coastal region of South America, the locations of the largest tsunami heights of both events are adjacent (Figure 4a), i.e., Coquimbo (the 2011 Tohoku) and Chañaral (The 2022 HTHH).

To further compare the far-field hydrodynamic processes between these two events quantitatively, we conduct wavelet analysis for four representative tide gauges distributed across the Pacific Ocean, i.e. coastal gauges at East Cape in New Zealand, Kwajalein Island, Wake Island, and Talcahuaho in Chile (see their locations in Figures 10b). The temporal changes of tsunami energy of both events can be seen in Figure 11. At each tide gauge, the tsunami energy of the 2011 HTHH (Figure 11a) and the 2022 Tohoku tsunamis (Figure 11b) for the first few hours after the arrivals is nonuniform with different significant peaks distributed within a wide period band of ~3–100 min. Then, the following long-lasting energy of the both at each station presents similar pattern and is concentrated at identical and fairly narrower period channel, i.e., ~20–30 min at East Cape in New Zealand, ~40–60 min at Kwajalein Island, ~10 min at Wake Island, and ~100 min at Talcahuaho in Chile, which reflects the local bathymetric effects of natural permanent oscillations (Hu et al., 2022; Satake et al., 2020). Specifically, many bathymetric effects can contribute to the long-lasting tsunami, such as multiple reflections across the basins, or the continental shelves, and the excited tsunami resonance in bays/harbors with variable shapes and sizes (Aranguiz et al., 2019; Satake et al., 2020). For example, tide gauges around New Zealand are primarily distributed in harbors/ports with major natural oscillation modes of ~20–30 min (De Lange and Healy, 1986; Lynett et al., 2022). The first oscillation mode of central Chile is centered around ~100 min (Aranguiz et al., 2019). Consequently, Figure 11 illustrates that the long-lasting tsunami energy of the two events is respectively distributed in 20–30 min period at East Cape in New Zealand and in ~100 min period at Talcahuaho in central Chile. The coupling of bathymetric oscillation mode with tsunami containing similar-period wave results in the excitement of tsunami resonance, which amplifies tsunami waves and prolongs the tsunami oscillation at the two stations (Heidarzadeh et al., 2019, 2021; Hu et al., 2022; Wang et al., 2022).

Simply put, we do not have clear evidence that atmospheric acoustic-gravity waves from the 2022 HTHH eruption directly contribute to the long-lasting tsunami, but the resonance effect associated with ocean waves could a possible source of increased wave energy and amplification. However, the similarity of far-filed hydrodynamic behaviors between the 2022 HTHH volcanic tsunami and the 2011 Tohoku seismogenic tsunami well demonstrates the both went through similar hydrodynamic processes after their arrivals. The consistency favors that the long-lasting tsunami of 2022 HTHH tsunami event can very likely be attributed by the interplays between local bathymetry and conventional tsunami left after each passage of atmospheric waves, which can well explain why the two completely distinct tsunami events possess a comparable duration time.

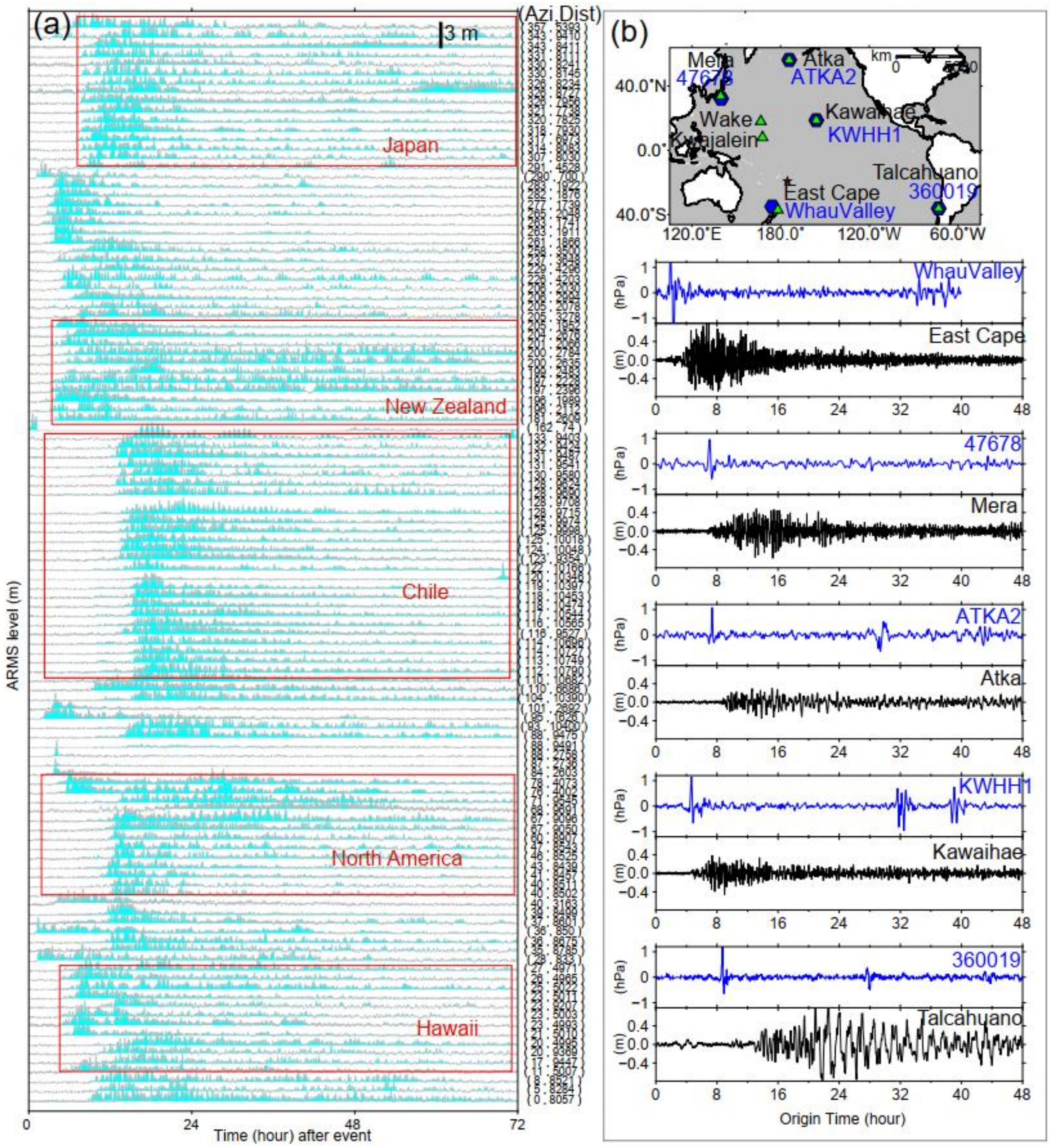

Figure 10. Tsunami duration. (a) Tsunami durations at Pacific 116 tide gauges through ARMS level approach. (b) the location of barographs (blue curves) and nearby tide gauges (green curves), as well as their waveforms.

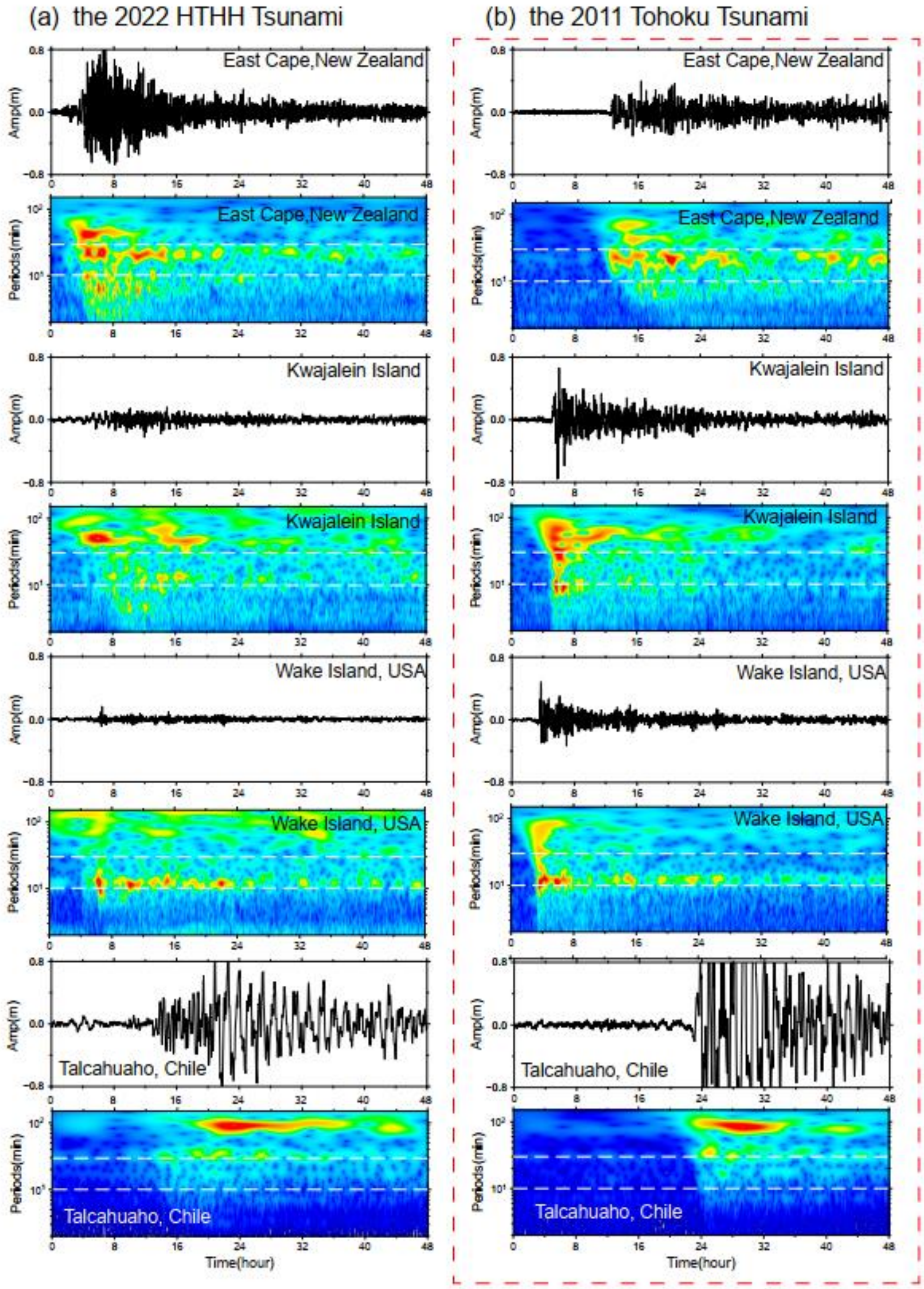

Figure 11. Wavelet analysis of tsunami waveforms recorded by 4 tide gauges during (a) the 2022 HTHH tsunami event, and (b) the 2011 Tohoku tsunami event. Horizontal white dashed lines respectively mark reference periods of 10 min and 30 min.

4.3 Challenges for Tsunami Warning

The generation mechanisms and hydrodynamic characteristics of the 2022 HTHH volcanic tsunami are more complicated than pure seismogenic tsunami, which challenge the traditional tsunami warning approach.

The first challenge is posed by the tsunami components with propagating velocities faster than the conventional tsunami. The Tonga volcanic tsunami event provides an excellent example which highlights that the tsunamigenic mechanisms are not limited to tectonic activities related with the sudden seafloor displacements, but also include a variety of atmospheric waves with distinct propagation velocities. The tsunami components in 2022 HTHH event generated by the air-sea coupling possess a wide range of velocities from 1000 m/s to 200 m/s. The Lamb waves recorded in both the 2022 HTHH event and the 1833 Krakatoa volcanic event traveled along the Earth's surface globally for several times (Carvajal et al., 2022). The tsunami waves produced by Lamb waves, the wave components associated with resonance of the air-sea coupling and their superimposition increase the difficulty of tsunami warning.

Another critical challenge is associated with the interplays between tsunami waves and local bathymetry. The tsunami waves left by each passage of the atmospheric waves can interact with local bathymetry at coastlines, such as continental shelves with different slopes, and harbor/bay with different shapes and sizes. The interaction can intensify the tsunami impact and excite a variety of natural oscillation periods. The 2022 HTHH tsunami with an extremely wide period range of ~2–100 min have a great potential to couple with the excited natural oscillations and form extensive tsunami resonance phenomena. The resonance effects result in long-lasting oscillation and delayed tsunami wave peaks. The uncertain arrivals of the maximum tsunami waves pose an extra challenge to tsunami warning.

5. Conclusion

In the study, we explore the tsunamigenic mechanisms and the hydrodynamic characteristics of the 2022 HTHH volcanic tsunami event. Through extensive analysis of waveforms recorded by the DART buoys, tide gauges and barometers in the Pacific Ocean, we reach the main findings as follows:

(1) We identify four distinct tsunami wave components based on their distinct propagation velocities or period bands (~80–100 min, 10–30 min, 30–40 min, and 3–5 min). The generation mechanisms of these tsunami components range from air-sea coupling to seafloor crustal deformation during the volcanic eruption.

(2) The first-arriving tsunami component with 80–100 min period was most likely from shock wave spreading at a velocity of ~1000 m/s in the vicinity of the eruption. This tsunami component was not clearly identified by currently available publication and it's not easy to be visually observed through time series of the waveforms. The physical mechanism is yet to be understood. The second tsunami component

with 30–40 min period was from Lamb waves, and was the most discussed tsunami source of this event so far. A thorough analysis of DART measurements indicates that the Lamb waves traveled at the speed of ~340 m/s in the vicinity of the eruption and decreased to ~315 m/s when traveling away due to cooling of the air temperature. The third tsunami component was from some atmospheric gravity wave modes with propagation velocity faster than 200 m/s but slower than Lamb waves. The last tsunami component with the shortest periods 3-5 min was probably produced by partial caldera collapse with estimated dimension of ~0.8–1.8 km.

(3) Although the resonance effect with the atmospheric acoustic-gravity waves could be a source of increased wave energy, its direct contribution to the long-lasting oscillation is not demonstrated yet. However, the comparison of hydrodynamical characteristics between the 2022 HTHH tsunami event and the 2011 Tohoku tsunami event well demonstrated that the interactions between the ocean waves left by atmospheric waves and local bathymetry contribute to the long-lasting Pacific oscillation of the 2022 tsunami event.

(4) The extraordinary features of this rare volcanic tsunami event challenge the current tsunami warning system which is mainly designed for seismogenic tsunamis. It is necessary to improve the awareness of people at risks about the potential tsunami hazards associated with volcanic eruptions. New approaches are expected to be developed for tsunami hazard assessments with these unusual sources: various atmospheric waves radiated by volcanic eruptions besides those traditionally recognized, e.g. earthquakes, landslides, caldera collapses and pyroclastic flows etc.

Acknowledgment

This work was supported by National Natural Science Foundation (No 41976197, No 12002099), Innovation Group Project of Southern Marine Science and Engineering Guangdong Laboratory (Zhuhai) (No. 311021002), Key Research and Development Program of Hainan Province (No. ZDYF2020209), Southern Marine Science and Engineering Guangdong Laboratory (Zhuhai) (SML2021SP305) and Fundamental Research Funds for the Central Universities, Sun Yat-sen University (2021qntd23).

The JAGURS tsunami simulation code is employed for tsunami modelling (Baba et al., 2015; https://zenodo.org/record/6118212#.Yk98qdtBxPY). Bathymetry data are obtained from GEBCO at http://www.gebco.net. The sea level records in deep ocean are available from the Deep Ocean Assessment

and Reporting of Tsunamis (DART) buoy network in the Pacific (https://nctr.pmel.noaa.gov/Dart/), and GeoNet New Zealand DART network (https://tilde.geonet.org.nz). The sea level records of tide gauges are downloaded from UNESCO/ IOC (http://www.ioc-sealevelmonitoring.org/). Barometer data are provided by the following providers: Direccio´n Meteorolo´gica de Chile (https://climatologia.meteochile.gob.cl), NOAA National Weather Service (https://www.weather.gov/ilm/observations), Japan Meteorological Agency (https://www.jma.go.jp), The UK Met Office Weather Observation (https://wow.metoffice.gov.uk/observations), and Fiji Meteorological Service (https://www.met.gov.fj).

Reference

Adam, D.: Tonga volcano created puzzling atmospheric ripples, Nature, https://doi.org/10.1038/d41586-022-00127-1, 2022.

Amores, A., Monserrat, S., Marcos, M., Argüeso, D., Villalonga, J., Jordà, G., and Gomis, D.: Numerical simulation of atmospheric Lamb waves generated by the 2022 Hunga-Tonga volcanic eruption, Geophys. Res. Lett., 49, e2022GL098240, https://doi.org/10.1029/2022GL098240, 2022.

Aranguiz, R., Catalán, P. A., Cecioni, C., Bellotti, G., Henriquez, P., and González, J.: Tsunami Resonance and Spatial Pattern of Natural Oscillation Modes With Multiple Resonators, J. Geophys. Res. Ocean., 124, 7797–7816, https://doi.org/10.1029/2019JC015206, 2019.

Baba, T., Takahashi, N., Kaneda, Y., Ando, K., Matsuoka, D., and Kato, T.: Parallel Implementation of Dispersive Tsunami Wave Modeling with a Nesting Algorithm for the 2011 Tohoku Tsunami, Pure Appl. Geophys., 172, 3455–3472, https://doi.org/10.1007/s00024-015-1049-2, 2015.

Bevis, M., Taylor, F. W., Schutz, B. E., Recy, J., Isacks, B. L., Helu, S., Singh, R., Kendrick, E., Stowell, J., Taylor, B., and Calmantli, S.: Geodetic observations of very rapid convergence and back-arc extension at the tonga arc, Nature, 374, 249–251, https://doi.org/10.1038/374249a0, 1995.

Billen, M. I., Gurnis, M., and Simons, M.: Multiscale dynamics of the Tonga–Kermadec subduction zone, Geophys. J. Int., 153, 359–388, https://doi.org/10.1046/j.1365-246X.2003.01915.x, 2003, 2003.

Carvajal, M., Sepúlveda, I., Gubler, A., and Garreaud, R.: Worldwide Signature of the 2022 Tonga Volcanic Tsunami, Geophys. Res. Lett., 49, e2022GL098153, https://doi.org/10.1029/2022GL098153, 2022.

Duncombe, J.: The Surprising Reach of Tonga's Giant Atmospheric Waves.pdf, Eos (Washington. DC)., 103, https://doi.org/10.1029/2022EO220050, 2022.

Edmonds, M.: Hunga-Tonga-Hunga-Ha'apai in the south Pacific erupts violently, Temblor, https://doi.org/10.32858/temblor.231, 2022.

Garvin, J. B., Slayback, D. A., Ferrini, V., Frawley, J., Giguere, C., Asrar, G. R., and Andersen, K.: Monitoring and Modeling the Rapid Evolution of Earth's Newest Volcanic Island: Hunga Tonga Hunga Ha'apai (Tonga) Using High Spatial Resolution Satellite Observations, Geophys. Res. Lett., 45, 3445–3452, https://doi.org/10.1002/2017GL076621, 2018.

Gossard, E. E. and Hooke, W. H.: Waves in the Atmosphere: Atmospheric Infrasound and Gravity Waves—Their Generation and Propagation, Elsevier, 1975a.

Gossard, E. E. and Hooke, W. H.: Waves in the Atmosphere, Amsterdam: Elsevier, 1975b.

Heidarzadeh, M. and Satake, K.: Waveform and Spectral Analyses of the 2011 Japan Tsunami Records on Tide Gauge and DART Stations Across the Pacific Ocean, Pure Appl. Geophys., 170, 1275–1293, https://doi.org/10.1007/s00024-012-0558-5, 2013.

Heidarzadeh, M. and Satake, K.: Excitation of Basin-Wide Modes of the Pacific Ocean Following the March 2011 Tohoku Tsunami, Pure Appl. Geophys., 171, 3405–3419, https://doi.org/10.1007/s00024-013-0731-5, 2014.

Hu, G., Feng, W., Wang, Y., Li, L., He, X., Karakaş, Ç., and Tian, Y.: Source characteristics and exacerbated tsunami hazard of the 2020 Mw 6.9 Samos earthquake in eastern Aegean Sea, J. Geophys. Res. Solid Earth, 127, e2022JB023961, https://doi.org/10.1029/2022JB023961, 2022.

Kawata, Y., Benson, B. C., Borrero, J. C., Borrero, J. L., Davies, H. L., Lange, W. P. de, Imamura, F., Letz, H., Nott, J., and Synolakis, C. E.: Tsunami in Papua New Guinea Was as Intense as First Thought, Eos, Trans. Am. Geophys. Union, 80, 9, https://doi.org/10.1029/99EO00065, 1999.

Kristeková, M., Kristek, J., Moczo, P., and Day, S. M.: Misfit Criteria for Quantitative Comparison of Seismograms, Bull. Seismol. Soc. Am., 96, 1836–1850, https://doi.org/10.1785/0120060012, 2006.

Kubota, T., Saito, T., and Nishida, K.: Global fast-traveling tsunamis by atmospheric pressure waves on the 2022 Tonga eruption, Science (80-.)., https://doi.org/10.1126/science.abo4364, 2022.

Kulichkov, S. N., Chunchuzov, I. P., Popov, O. E., Gorchakov, G. I., Mishenin, A. A., Perepelkin, V. G., Bush, G. A., Skorokhod, A. I., Yu. A. Vinogradov, Semutnikova, E. G., Šepic, J., Medvedev, I. P., Gushchin, R. A., Kopeikin, V. M., Belikov, I. B., Gubanova, D. P., and A. V. Karpov & A. V. Tikhonov: Acoustic-Gravity Lamb Waves from the Eruption of the Hunga-Tonga-Hunga-Hapai Volcano, Its Energy Release and Impact on Aerosol Concentrations and Tsunami, Pure Appl. Geophys., https://doi.org/10.1007/s00024-022-03046-4, 2022.

Lamb, H.: Hydrodynamics, Cambridge Univ. Press, 1932.

De Lange, W. P. and Healy, T. R.: New Zealand tsunamis 1840–1982, New Zeal. J. Geol. Geophys., 29, 115–134, https://doi.org/10.1080/00288306.1986.10427527, 1986.

Lin, J., Rajesh, P. K., Lin, C. C. H., Chou, M., Liu, J.-Y., Yue, J., Hsiao, T.-Y., Tsai, H.-F., Chao, H.-M., and Kung, M.-M.: Rapid Conjugate Appearance of the Giant Ionospheric Lamb Wave Signatures in the Northern Hemisphere After Hunga- Tonga Volcano Eruptions, Geophys. Res. Lett., 49, e2022GL098222, https://doi.org/10.1029/2022GL098222, 2022.

Liu, P. L.-F. and Higuera, P.: Water waves generated by moving atmospheric pressure : Theoretical analyses with applications to the 2022 Tonga event, arXiv Prepr., https://doi.org/10.48550/arXiv.2205.05856, 2022.

Liu, X., Xu, J., Yue, J., and Kogure, M.: Strong Gravity Waves Associated With Tonga Volcano Eruption Revealed by SABER Observations, Geophys. Res. Lett., 49, e2022GL098339, https://doi.org/10.1029/2022GL098339, 2022.

Lynett, P., McCann, M., Zhou, Z., Renteria, W., Borrero, J., Greer, D., Fa'anunu, 'Ofa, Bosserelle, C., Jaffe, B., Selle, S. La, Ritchie, A., Snyder, A., Nasr, B., Bott, J., Graehl, N., Synolakis, C., Ebrahimi, B., and Cinar, G. E.: Diverse tsunamigenesis triggered by the Hunga Tonga-Hunga Ha'apai eruption, Nature, 609, 728–733, https://doi.org/10.1038/s41586-022-05170-6, 2022.

Matoza, R. S., Matoza, R. S., Fee, D., Assink, J. D., Iezzi, A. M., Green, D. N., Kim, K., Lecocq, T., Krishnamoorthy, S., Lalande, J., Nishida, K., and Gee, K. L.: Atmospheric waves and global seismoacoustic observations of the January 2022 Hunga eruption ,Tonga, Science (80-.)., https://doi.org/10.1126/science.abo7063, 2022.

Mori, N., Takahashi, T., Yasuda, T., and Yanagisawa, H.: Survey of 2011 Tohoku earthquake tsunami inundation and run-up, Geophys. Res. Lett., 38, L00G14, https://doi.org/10.1029/2011GL049210, 2011.

NASA: National Aeronautics and Space Administration,"Dramatic changes at Hunga Tonga-Hunga

Ha'apai," 2022.
Nomanbhoy, N. and Satake, K.: Generation mechanism of tsunamis from the 1883 Krakatau Eruption, Geophys. Res. Lett., 22, 509–512, https://doi.org/10.1029/94GL03219, 1995.
Omira, R., Baptista, M. A., Quartau, R., Ramalho, R. S., Kim, J., Ramalho, I., and Rodrigues, A.: How hazardous are tsunamis triggered by small-scale mass-wasting events on volcanic islands ? New insights from Madeira–NE Atlantic, Earth Planet. Sci. Lett., 578, 117333, https://doi.org/10.1016/j.epsl.2021.117333, 2022.
Otsuka, S.: Visualizing Lamb Waves From a Volcanic Eruption Using Meteorological Satellite Himawari-8, Geophys. Res. Lett., 49, e2022GL098324, https://doi.org/10.1029/2022GL098324, 2022.
Pelinovsky, E., Choi, B. H., Stromkov, A., Didenkulova, I., and Kim, H.: Analysis of Tide-Gauge Records of the 1883 Krakatau Tsunami. In: Satake, K. (eds) Tsunamis, Adv. Nat. Technol. Hazards Res., 23, Springer, Dordrech, https://doi.org/10.1007/1-4020-3331-1_4, 2005.
Le Pichon, A., Blanc, E., and Hauchecorne, A.: Infrasound monitoring for atmospheric studies, Springer Science & Business Media, 1–735 pp., https://doi.org/10.1007/978-1-4020-9508-5, 2010.
Plank, S., Marchese, F., Genzano, N., Nolde, M., and Martinis, S.: The short life of the volcanic island New Late'iki (Tonga) analyzed by multi-sensor remote sensing data, Sci. Rep., 10, 22293, https://doi.org/10.1038/s41598-020-79261-7, 2020.
Rabinovich, A. B.: Spectral analysis of tsunami waves: Separation of source and topography effects, J. Geophys. Res. Ocean., 102, 12663–12676, https://doi.org/10.1029/97JC00479, 1997.
Rabinovich, A. B.: Seiches and harbor oscillations. in: Handbook of coastal and ocean engineering, pp, 193–236, 2009.
Rabinovich, A. B., Thomson, Æ. R. E., and Stephenson, F. E.: The Sumatra tsunami of 26 December 2004 as observed in the North Pacific and North Atlantic oceans, Surv. Geophys., 27, 647–677, https://doi.org/10.1007/s10712-006-9000-9, 2006.
Rabinovich, A. B., Titov, V. V., Moore, C. W., and Eble, M. C.: The 2004 Sumatra Tsunami in the Southeastern Pacific Ocean: New Global Insight From Observations and Modeling, J. Geophys. Res. Ocean., 122, 7992–8019, https://doi.org/https://doi.org/10.1002/2017JC013078, 2017.
Ramalho, R. S., Winckler, G., Madeira, J., Helffrich, G. R., Hipólito, A., Quartau, R., Adena, K., and Schaefer, J. M.: Hazard potential of volcanic flank collapses raised by new megatsunami evidence, Sci.

Adv., 1, e1500456, https://doi.org/10.1126/sciadv.1500456, 2015.

Ramírez-Herrera, M. T., Coca, O., and Vargas-Espinosa, V.: Tsunami Effects on the Coast of Mexico by the Hunga Tonga-Hunga Ha'apai Volcano, Pure Appl. Geophys., https://doi.org/10.1007/s00024-022-03017-9, 2022.

Satake, K.: Earthquakes: Double trouble at Tonga, Nature, 466, 931–932, https://doi.org/10.1038/466931a, 2010.

Satake, K., Heidarzadeh, M., Quiroz, M., and Cienfuegos, R.: History and features of trans-oceanic tsunamis and implications for paleo-tsunami studies, Earth-Science Rev., 202, 103112, https://doi.org/10.1016/j.earscirev.2020.103112, 2020.

Self, S. and Rampino, M. R.: K-1981Self_Nature_The 1883 eruption of Krakatau, Nature, 294, 699–704, https://doi.org/10.1038/294699a0, 1981.

Stern, S., Cronin, S., Ribo, M., Barker, S., Brenna, M., Smith, I. E. M., Ford, M., Kula, T., and Vaiomounga, R.: Post-2015 caldera morphology of the Hunga Tonga-Hunga Ha ' apai caldera , Tonga , through drone photogrammetry and summit area bathymetry, EGU Gen. Assem. 2022, https://doi.org/10.5194/egusphere-egu22-13586, 2022.

Themens, D. R., Watson, C., Žagar, N., Vasylkevych, S., Elvidge, S., McCaffrey, A., Prikryl, P., Reid, B., Wood, A., and Jayachandran, P. T.: Global Propagation of Ionospheric Disturbances Associated With the 2022 Tonga Volcanic Eruption, Geophys. Res. Lett., 49, e2022GL098158, https://doi.org/10.1029/2022GL098158, 2022.

Thomson, R. E. and Emery, W. J.: Data Analysis Methods in Physical Oceanography: Third Edition, New York: Elsevier, 1–716 pp., 2014.

Titov, V., Rabinovich, A. B., Mofjeld, H. O., Thomson, R. E., and Gonza, F. I.: The Global Reach of the 26 December 2004 Sumatra Tsunami, Science (80-.)., 309, 2045–2049, https://doi.org/10.1126/science.1114576, 2005.

USGS: M 5.8 Volcanic Eruption - 68 km NNW of Nuku'alofa, Tonga, U.S. Geol. Surv., 2022.

Wang, Y., Heidarzadeh, M., Satake, K., Mulia, I. E., and Yamada, M.: A Tsunami Warning System Based on Offshore Bottom Pressure Gauges and Data Assimilation for Crete Island in the Eastern Mediterranean Basin, J. Geophys. Res. Solid Earth, 125, e2020JB020293, https://doi.org/10.1029/2020JB020293, 2020.

Wang, Y., Zamora, N., Quiroz, M., Satake, K., and Cienfuegos, R.: Tsunami Resonance Characterization in Japan Due to Trans-Pacific Sources: Response on the Bay and Continental Shelf, J. Geophys. Res. Ocean., 126, 1–16, https://doi.org/10.1029/2020JC017037, 2021.

Wang, Y., Heidarzadeh, M., Satake, K., and Hu, G.: Characteristics of two tsunamis generated by successive Mw 7.4 and Mw 8.1 earthquakes in Kermadec Islands on March 4,2021, Nat. Hazards Earth Syst. Sci., 22, 1–10, https://doi.org/10.5194/nhess-2021-369, 2022.

Watanabe, S., Hamilton, K., Sakazaki, T., and Nakano, M.: First Detection of the Pekeris Internal Global Atmospheric Resonance: Evidence from the 2022 Tonga Eruption and from Global Reanalysis Data, J. Atmos. Sci., 79, 3027–3043, https://doi.org/10.1175/jas-d-22-0078.1, 2022.

Yuen, D. A., Scruggs, M. A., Spera, F. J., Yingcai Zheng, Hao Hu, McNutt, S. R., Glenn Thompson, Mandli, K., Keller, B. R., Wei, S. S., Peng, Z., Zhou, Z., Mulargia, F., and Tanioka1, Y.: Under the Surface: Pressure-Induced Planetary-Scale Waves, Volcanic Lightning, and Gaseous Clouds Caused by the Submarine Eruption of Hunga Tonga-Hunga Ha'apai Volcano Provide an Excellent Research Opportunity, Earthq. Res. Adv., https://doi.org/10.1016/j.eqrea.2022.100134, 2022.

Zhang, S., Vierinen, J., Aa, E., Goncharenko, L. P., Erickson, P. J., Rideout, W., Coster, A. J., and Spicher, A.: 2022 Tonga Volcanic Eruption Induced Global Propagation of Ionospheric Disturbances via Lamb Waves, Front. Astron. Sp. Sci., 9, 1–10, https://doi.org/10.3389/fspas.2022.871275, 2022.